Journal of Ceramic Processing Research. Vol. 14, No. 5, pp. 610~615 (2013)

JOURNAL OF
Ceramic
Processing Research

Mechanical properties and high speed machining characteristics of Al_2O_3-based ceramics for dental implants

D. Tang[a], H.B. Lim[a], K.J. Lee[a], S.J. Ha[b], K.B. Kim[b], M.W. Cho[b], K. Park[c] and W.S. Cho[a,*]
[a]*School of Materials Science & Eng., Inha University, Incheon 402-751, Korea*
[b]*Department of Mechanical Engineering, Inha University, Incheon 402-751, Korea*
[c]*Nanotechnology and Advanced Materials Engineering, Sejong University, Seoul 143-741, Korea*

This study examined the effect of the 3Y-TZP (3 mol% yttria stabilized tetragonal zirconia polycrystal) content on the mechanical properties and machinability of Al_2O_3 ceramics. The fracture toughness and biaxial strength increased with increasing 3Y-TZP content. The increasing amount of tetragonal ZrO_2 and finer grain size of Al_2O_3 appear to be responsible for the high fracture toughness and biaxial strength, respectively. The thermal-induced residual stresses that probably account for the enhancement of fracture toughness were also calculated. The cutting force for a fully densified Al_2O_3 ceramic decreased with decreasing depth of cut or increasing cutting speed. Severe tool wear was observed during the cutting process due to the high hardness of the fully densified Al_2O_3 ceramic.

Key words: Ceramics. Composites, Sintering, Machining, Microstructure, Strength.

Introduction

Alumina (Al_2O_3) ceramics are used widely as structural engineering materials in the field of advanced ceramics. The properties of Al_2O_3 ceramics, such as high hardness, abrasion resistance and chemical inertness, have attracted considerable interest for applications in the dental crown [1]. Al_2O_3 was first introduced as a dental material in the 1970s but early clinical applications revealed a high fracture rate of 13%. The second, improved generation of Al_2O_3 ceramics, which was developed in the late 1980s, presented smaller grains and higher density with a < 5% failure rate. The third generation of Al_2O_3 with finer microstructures showed improved properties [2, 3]. Despite the improved properties of Al_2O_3 ceramic, its brittleness has limited its applications in dental implants. Ceramic restorations are used cautiously because they are susceptible to crack propagation under high compression conditions in impact areas. Thus, dental implants with high fracture toughness and fracture strength are required [4].

The concept of toughening Al_2O_3 ceramics by dispersing zirconia (ZrO_2) particles in the matrix has been proposed [5]. The toughening of Al_2O_3 by ZrO_2 particles can be attributed to the tetragonal to monoclinic phase transformation of ZrO_2. The volume expansion and shear strain associated with this transformation results in compressive stress that may develop on a ground surface or in the vicinity of a crack tip. Cracks must overcome this clamping constraint on the crack tip to propagate, which can explain the enhanced fracture resistance of the composites [6]. Therefore, the Al_2O_3-ZrO_2 system, which consists of ZrO_2-toughened Al_2O_3 (ZTA) ceramics and Al_2O_3-toughened ZrO_2 ceramics (ATZ), has attracted increasing interest as a potential alternative for both Al_2O_3 and ZrO_2 monoliths [7]. Although, the microstructural evolution of Al_2O_3-ZrO_2 ceramics has been investigated, there are still discrepant results regarding the effect of addition of ZrO_2 in Al_2O_3 or Al_2O_3 in ZrO_2 on the mechanical properties [4, 5, 8, 9]. These discrepancies can be due to differences in the starting powder, sintering temperature, sintering time and processing methods, which can affect the final microstructure.

On the other hand, computer-aided design and computer-aided manufacturing (CAD/CAM) technologies are used to prepare ceramic restorations in dentistry [10]. The desired shapes for dental implants are obtained fairly rapidly using either a milling cutter or an abrasive tool depending on the machining properties of the workpiece material [11]. The literature shows that very few data are available on the end-mill machining of fully densified ceramics. This is due to the experimental difficulties involved in machining ceramics with high hardness and low fracture toughness. Nevertheless, it is important to determine the factors related to the machining properties of the fully densified ceramics.

In this study, the effects of the ZrO_2 content on the

*Corresponding author:
Tel : +82-32-860-7528
Fax: +82-32-862-5546
E-mail: wscho@inha.ac.kr

mechanical properties of Al_2O_3 ceramics investigated over a wide range of ZrO_2 contents from 0 vol% to 80 vol% to produce composites with the properties required for dental implants. In addition, the high speed machining characteristics of fully-densified Al_2O_3 ceramics were examined. The machinability of the Al_2O_3 ceramic was evaluated in an end-milling process under a range of cutting conditions, such as cutting speed and depth of cut variations.

Experimental Procedures

Preparation of composites

High purity Al_2O_3 (TM-DAR, α-Al_2O_3, > 99.99%, 0.1 μm, TAIMEI, Japan) and 3 mol% yttria stabilized tetragonal zirconia polycrystal (3Y-TZP, TZ-3YSB-E, 90 nm, Tosho, Japan) were used as the raw powders. Al_2O_3 based ceramic composites with different 3Y-TZP contents (0 vol%, 20 vol%, 40 vol%, 60 vol% and 80 vol%) were prepared. The mixed powders were ball-milled for 24 hrs in an ethanol medium using a plastic jar with Al_2O_3 balls. The slurries were dried simultaneously using rotary evaporator. After drying and sieving, the powders were pressed uniaxially into rectangular and disk green bodies at 100 MPa, and cold isostatic pressed (CIP) at 150 MPa. The obtained green compacts were then sintered at 1600 °C for 2 h in air. After grinding (400 grit diamond wheel) and polishing (1 μm diamond paste), rectangular specimens with dimensions of $3 \times 4 \times 40$ (mm) and disc specimens with a diameter and thickness of 16 mm and 1.6 mm, respectively, were obtained. The specimens were annealed at 1200 °C in order to remove any residual stresses. Rectangular Al_2O_3 monolith specimens with dimensions of $40 \times 20 \times 10$ mm were fabricated to evaluate the machining characteristics.

Microstructure and mechanical properties characterization

Crystalline phase analysis was carried out by X-ray diffraction (XRD, DMAX-2500, Rigaku) using Cu Kα radiation in the 2θ range, 20°-80° at a scanning rate of 2°/min. The microstructures of all composites were observed by SEM after thermal etching at 1500 °C for 1 hr. The fracture toughness was measured using the single-edge V-notched beam (SEVNB) method. Ground and polished rectangular specimens ($3 \times 4 \times 40$ mm) were notched on the surface (3×40 mm) using a diamond charged cutting wheel, perpendicular to the length of the rectangular bars. The depth of the notches was approximately 0.7 mm, which is $\leq$ 20% of the height of the specimen according to the DIN standard [12]. The notches were sharpened with a razor blade machine using a diamond paste filled into the notch. The sharpened notch root radius of the prepared specimen was less than 20 μm. The fracture strength of the specimens was then measured using a four-point flexure test. To measure the Vickers hardness, the specimens were polished to a mirror-like finish and indentations were introduced on the surface of each composition using a Vickers hardness testing machine (Akashi, Model, AVK-C0) under a 98N load at a dwell time of 15s. The biaxial flexural strength was evaluated using piston-on-three-ball test [13]. The disc type specimens were ruptured using a universal testing machine at a cross head speed of 0.5 mm/min.

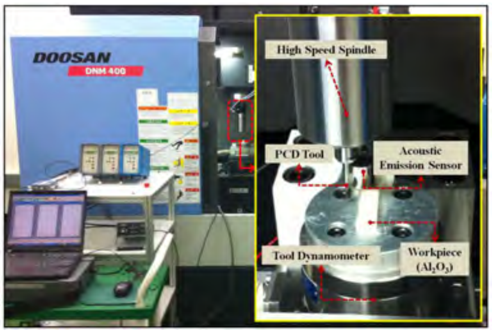

Fig. 1. Photograph of the cutting experiment setup.

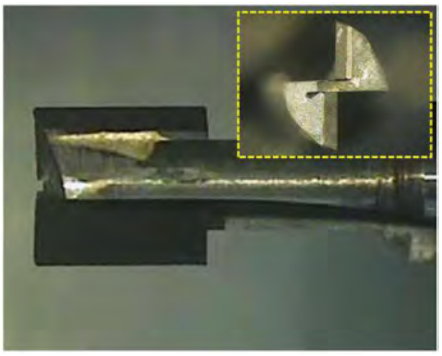

Fig. 2. Photographs of PCD milling tool used for the experiments.

Table 1. Properties of the polycrystalline diamond (PCD).

Grain size (μm)	Hardness (kg/mm^2)	Young's modulus (GPa)	Thermal conductivity (W/mK)
	6,000 ~ 9,000	800 ~ 900	100 ~ 550

Machining characteristics

Fig. 1 shows the CNC vertical milling machine and monitoring systems used for the experiments. The machining experiments were carried out on a Doosan CNC machining center (DNM 400). A high-speed spindle with an electric motor and air bearing was mounted on the spindle of the CNC milling machine. The maximum rotational speed of the installed high-speed spindle was 100,000 rpm. To evaluate the machinability of the Al_2O_3, a series of experiments were performed using two-fluted polycrystalline diamond (PCD) milling tools, 6 mm in diameter. Fig. 2 shows images of the PCD tool used for the experiments. Table 1 lists the material properties of the PCD. The implemented cutting force measurement

Table 2. Cutting conditions for the Al_2O_3 monolithic ceramics.

Tool type	Depth of cut (mm)	Cutting speed (rpm)	Feedrate (mm/min)
two-Flat, 6 mm diameter	0.01, 0.05, 0.1	20,000, 40,000, 60,000	50

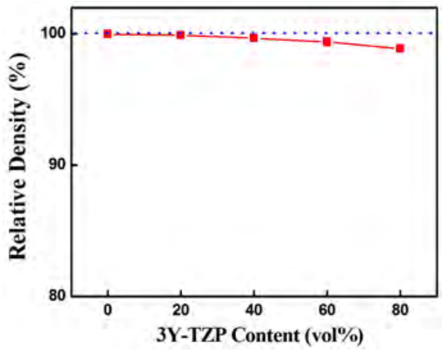

Fig. 3. Relative density of the Al_2O_3/3Y-TZP composites as a function of the 3Y-TZP content.

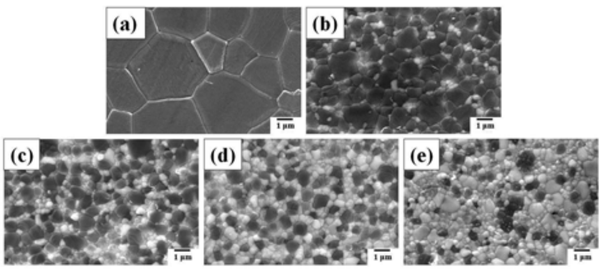

Fig. 4. SEM images of the Al_2O_3/3Y-TZP composites as a function of the 3Y-TZP content: (a) Al_2O_3, (b) Al_2O_3/20 vol% 3Y-TZP, (c) Al_2O_3/40 vol% 3Y-TZP, (d) Al_2O_3/60 vol% 3Y-TZP, (e) Al_2O_3/80 vol% 3Y-TZP.

system was composed of a piezo type tool dynamometer and acoustic emission (AE) sensors. The tool dynamometer was placed under the workpiece, and an acoustic emission sensor was attached to the workpiece. The sensor signals were acquired simultaneously through an A/D conversion board. Table 2 lists the cutting conditions used for the experiment.

Results and discussion

Fig. 3 shows the relative density of the Al_2O_3/3Y-TZP composites as a function of the 3Y-TZP content. The relative densities of all composites were > 98.9%. The relative densities decreased slightly with increasing 3Y-TZP content, indicating that the addition of 3Y-TZP inhibits the densification of Al_2O_3.

Fig. 4 presents SEM images of the polished and thermally etched Al_2O_3/3Y-TZP composites with various 3Y-TZP contents. Al_2O_3 (the darker phase) and ZrO_2 (the brighter phase) could be observed clearly. For the ZTA composites (3Y-TZP content less than 50 vol%), the ZrO_2 particles were dispersed homogeneously in the Al_2O_3 matrix, which were located at the triple

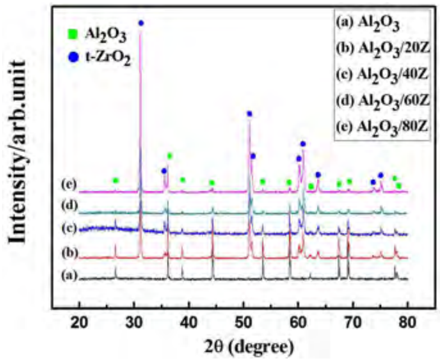

Fig. 5. XRD patterns of the Al_2O_3/3Y-TZP composites: (a) Al_2O_3, (b) Al_2O_3/20 vol% 3Y-TZP, (c) Al_2O_3/40 vol% 3Y-TZP, (d) Al_2O_3/60 vol% 3Y-TZP, (e) Al_2O_3/80 vol% 3Y-TZP.

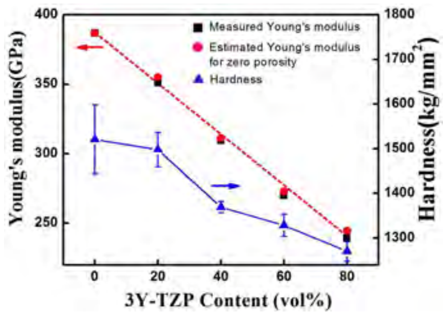

Fig. 6. Elastic modulus and hardness of the Al_2O_3/3Y-TZP composites as a function of the 3Y-TZP content.

junction and grain boundary of Al_2O_3. The grain size of Al_2O_3 decreased with increasing 3Y-TZP content from 1.61 μm for the Al_2O_3 ceramic to 0.81 μm for the Al_2O_3/40 vol% 3Y-TZP ceramic, indicating that ZrO_2 acts as a grain growth inhibitor. In ATZ composites (3Y-TZP content > 50 vol%), the grain size of Al_2O_3 decreased with increasing 3Y-TZP content from 0.725 μm for the Al_2O_3/60 vol% 3Y-TZP ceramic to 0.5 μm for the Al_2O_3/80 vol% 3Y-TZP ceramic, whereas the grain size of ZrO_2 were approximately 0.5 μm in both ATZ composites. Al_2O_3 particles were distributed in a fine grain 3Y-TZP matrix.

Fig. 5 shows XRD patterns of the ZTA and ATZ composites. α-Al_2O_3 and tetragonal ZrO_2 were observed. Tetragonal ZrO_2 was fully retained in all composites. The absence of monoclinic ZrO_2 indicates that Al_2O_3 has no effect on the phase transformation of ZrO_2 during sintering.

Fig. 6 shows the hardness and elastic modulus of the composites. The measured elastic modulus decreased with increasing 3Y-TZP content from 0 to 80 vol%. This is reasonable considering that the elastic modulus of Al_2O_3 (400 GPa) is much higher than that of ZrO_2 (192 GPa) [14, 15]. In ceramic matrix composites, the elastic modulus obeyed the linear rule of mixtures [6], which can be explained by Eq. (1):

$$E_C = E_A V_A + E_Z V_Z \quad (1)$$

where E_c is the elastic modulus of the Al_2O_3/3Y-TZP composites, E_A is the elastic modulus of Al_2O_3, E_Z is the elastic modulus of 3Y-TZP, and V_A and V_Z are the volume fraction of Al_2O_3 and 3Y-TZP, respectively. As shown in Fig. 6, the experimental values were consistent with the linear rule of mixtures (dotted line). The elastic modulus decreased with increasing volume faction of porosity, as shown by following relationship (2) [16]:

$$E=E_0(1-1.9p+0.9p^2) \tag{2}$$

where E is the elastic modulus of the porous ceramic, E_0 is the elastic modulus of the nonporous ceramic and P is the porosity. The elastic moduli for zero porosity were estimated using Eq. (2). The estimated moduli were higher than the experimental values. The hardness of the Al_2O_3 decreased with increasing 3Y-TZP content, varying from 1,520 kg/mm^2 for the monolithic Al_2O_3 ceramic to 1,270 kg/mm^2 for the Al_2O_3 ceramic containing 80 vol% 3Y-TZP.

Fig. 7 shows the biaxial strength and fracture toughness of the Al_2O_3/3Y-TZP composites as a function of the 3Y-TZP content. All specimens were polished carefully and annealed at 1200 °C for 1 hr to eliminate the residual stress and transformed layer generated during the polishing procedure. The fracture toughness increased with increasing 3Y-TZP content ranging from 0 vol% to 80 vol%, varying from 6.4 to 11.2 MPa · m$^{1/2}$. This enhancement in fracture toughness indicates that an increasing amount of tetragonal ZrO_2 generally results in a considerable increase in fracture toughness of the

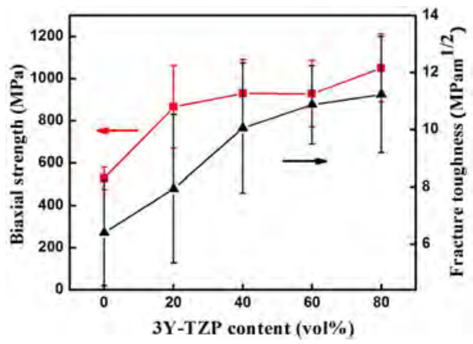

Fig. 7. Biaxial strength and fracture toughness of the Al_2O_3/3Y-TZP composites as a function of the 3Y-TZP content.

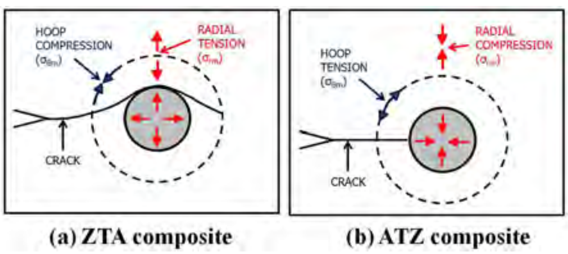

Fig. 8. Schematic diagram for the residual stress in the ZTA and ATZ composite due to thermal expansion mismatch between 3Y-TZP (10.3×10^{-6}/°C) and Al_2O_3 (8.1×10^{-6}/°C); (a) radial tensile stress and hoop compressive stress developed in the ZTA composites, (b) radial compressive stress and hoop tensile stress developed in the ATZ composites.

resulting Al_2O_3 ceramic. This can be explained by the stress-induced, tetragonal to monoclinic phase transformation of ZrO_2. The transformation-induced volume expansion generates a compressive stress field that impedes crack propagation and an extra load (or work) should be supplied for further crack propagation [17, 18]. The biaxial strength also shows increasing tendency with increasing 3Y-TZP content. The strength of ceramics depends not only on the fracture energy, fracture origin and Young's modulus, but also on the microstructure, such as grain size. A finer grain size results in higher fracture strength. The enhanced biaxial strength of the composites can be attributed to the refinement of grain size in both ZrO_2 and Al_2O_3.

In addition to the well established transformation toughening mechanism, the effect of residual stress on the mechanical properties of the ZrO_2-based ceramics should be investigated. Thermal-induced residual stress is generated during the cooling stage due to mismatch of the thermal expansion coefficient between ZrO_2 and Al_2O_3 [19]. The expansion coefficients of ZrO_2 and Al_2O_3 are 10.3×10^{-6}/°C and 8.1×10^{-6}/°C, respectively. Fig. 8 shows a schematic diagram of the residual stresses developed in a ZTA composite (Fig. 8(a)) and ATZ composite (Fig. 8(b)). In the ZTA composites, radial tensile stress and hoop compressive stress were generated. In such a case, a crack is deflected away from the 3Y-TZP particles, resulting in a tortuous crack path, as shown in Fig. 8(a). In contrast, radial compressive stress (σ_{rm}) and hoop tensile stress developed in the ATZ composites. The crack advances in the linear direction, as shown in Fig. 8(b).

The radial compressive stress (σ_{rm}) and the hoop tensile stress ($\sigma_{\theta m}$) are described by Eq. (3) and (4), respectively, as follows [20]:

$$\sigma_{rm}=\frac{P}{1-V_p}\left(\frac{a^3}{r^3}-V_p\right), V_p=\left(\frac{a}{b}\right)^3 \tag{3}$$

$$\sigma_{\theta m}=-\frac{P}{1-V_p}\left(\frac{1}{2}\frac{a^3}{r^3}+V_p\right) \tag{4}$$

Here, a is the particle radius, b is the matrix radius, r is the distance, V_p is the volume fraction of the particle in the matrix and P is the interfacial pressure, which can be evaluated by the Eq. (5) [20]:

$$P=(a_m-a_p)\Delta T/\left[\frac{0.5(1+v_m)+(1-2v_m)V_p}{E_m(1-V_p)}+\frac{1-2_p}{E_p}\right],$$
$$\Delta T=-1200°C \tag{5}$$

Fig. 9 shows the calculated residual stress in the ZTA and ATZ composites as a function of the 3Y-TZP content. The radial distance, r, away from the center of the particle was normalized to the particle radius (r_P). In the ZTA composites, the hoop compressive stress ($\sigma_{\theta m}$) at the interface between the particle and matrix

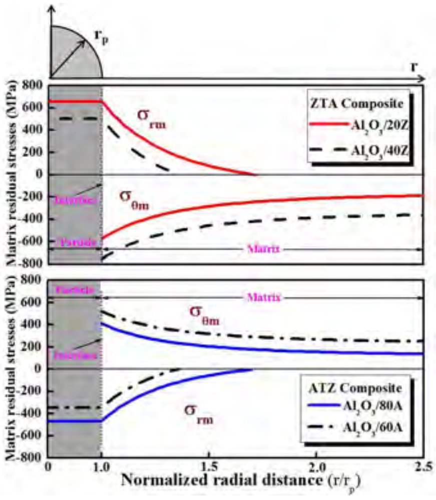

Fig. 9. Calculated radial and hoop stresses in the ZTA and ATZ composites as a function of the 3Y-TZP content. The radial distance was normalized by dividing the particle radius.

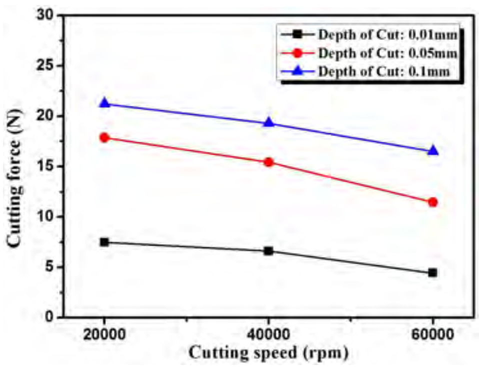

Fig. 10. Measured cutting forces according to the cutting condition variations.

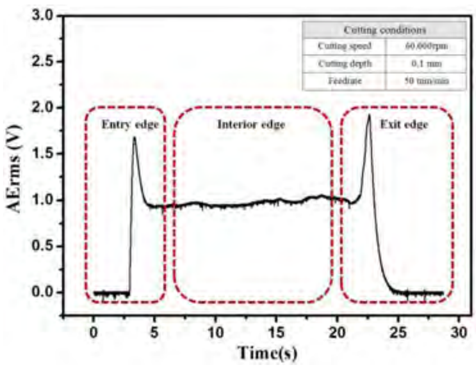

Fig. 11. AE signals were measured when rpm = 60,000, depth of cut = 0.1 mm, and feedrate = 50 mm/min.

increased with increasing 3Y-TZP content. For example, the hoop compressive stress increased from 574 MPa for Al_2O_3 containing 20 vol% 3Y-TZP to 754 MPa for Al_2O_3 containing 40 vol% 3Y-TZP. When the distance was larger than the particle radius ($r > r_p$), both the radial tensile stress and hoop compressive stress decreased with distance. The residual hoop compressive stress that developed in the ZTA composites probably accounts for the enhancement of strength and

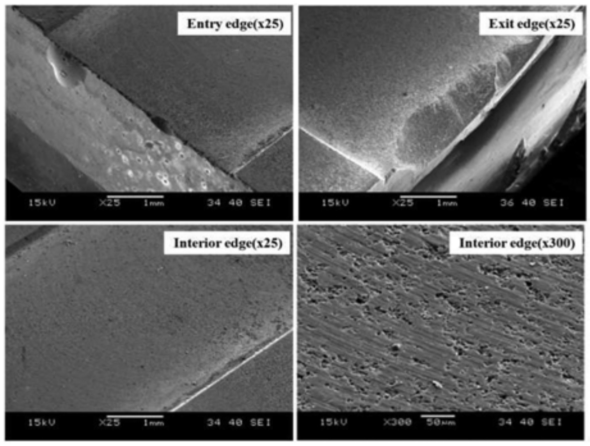

Fig. 12. SEM images of the machined surface when the cutting speed = 60,000 rpm, depth of cut = 0.1 mm, and federate = 50 mm/min.

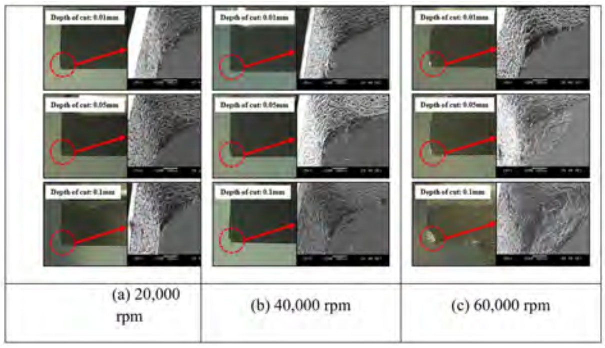

Fig. 13. Worn edges of the PCD tools according to the cutting conditions.

fracture toughness, as well as for the higher tendency of crack deflection.

In the ATZ composites, the hoop tensile stress ($\sigma_{\theta m}$) at the interface between the particle and the matrix decreased with increasing 3Y-TZP content. The hoop tensile stress decreased from 520 MPa for Al_2O_3 containing 60 vol% 3Y-TZP to 410 MPa for Al_2O_3 containing 80 vol% 3Y-TZP. Both the radial tensile stress and hoop compressive stress decreased with the distance when the distance was larger than the particle radius ($r > r_p$). Crack deflection cannot be expected under such tensile residual stress. The fracture toughness of ZTA composites increased rapidly with increasing 3Y-TZP content (Fig. 7), but the increase in toughness was lower in the ATZ composites. The rapid increase in toughness of the ZTA composites can be explained by the combined mechanisms of phase transformation toughening and residual compressive stress in the matrix. With increasing 3Y-TZP content (> 50 vol%), the residual stress changed from compression to tension. As a result, the residual tensile stress in the ATZ composite can offset the beneficial transformation toughening contribution by ZrO_2.

The machinability was evaluated by examining the high speed machining characteristics for the fully-densified Al_2O_3 ceramic using PCD tools with high hardness. Fig. 10 shows the measured cutting force variations as a function of the cutting speed and depth of cut. The cutting force increased with increasing depth of cut but an increase in cutting speed causes a decrease in cutting force.

The acoustic emission (AE) signals were measured to examine edge chippings during ceramic machining (Fig. 11). The AE signals were measured at a cutting speed of 60,000 rpm, depth of cut of 0.1 mm, and feed rate of 50 mm/min. Three types of signals were observed during the cutting process, which were due to the different machining regions of the Al_2O_3 ceramic. First, entry edge chipping occurs at the entrance when the PCD tool initially contacts the ceramic, and is caused mainly by the impact of cutting tool. Second, middle edge chipping occurs along the tool path, which is due to the brittle nature of the ceramic. Third, exit edge chipping occurs when the PCD tool leaves the ceramic, and is related to the loss of material support at the exit edge [21]. Therefore, the exit edge was chipped away due to the eruption of stress. After the cutting process, the surface cracks generated during the cutting process were examined by SEM, as shown in Fig. 12.

Although the hardness of the PCD tools used for ceramic cutting is quite high, severe tool wear is inevitable during the cutting process because the hardness of the fully densified Al_2O_3 ceramic is also high. Fig. 13 shows images of the worn edges of the PCD tools according to the different cutting conditions. From the figures, the increased depth of the cut causes more tool wear due to the increase in cutting resistance (see Fig. 10). In addition, the increase in cutting speed can cause premature wear of the tools. This is due to the attached chips of the ceramic adhered to the PCD tools during the cutting process [22]. Future studies should examine the machinability of partially-sintered Al_2O_3 ceramic composites.

Conclusions

The mechanical properties and machinability of Al_2O_3 ceramics with 3Y-TZP contents ranging from 0 to 80 vol% were investigated. The biaxial strength of Al_2O_3 was increased significantly by the addition of 3Y-TZP. The refinement of the Al_2O_3 grains accounts for the enhanced biaxial strength of the Al_2O_3/3Y-TZP ceramic composites. The fracture toughness of the ZTA composites increased rapidly with increasing 3Y-TZP content but the increase in toughness was lower in the ATZ composites. The rapid increase in toughness in the ZTA composites can be explained by the combined mechanisms of phase transformation toughening and residual compressive stress. The residual tensile stress in the ATZ composite counteracted the beneficial transformation toughening contribution by ZrO_2. The cutting force for the fully densified Al_2O_3 ceramic decreased with decreasing depth of cut or increasing cutting speed. Severe tool wear was observed during the cutting process due to the high hardness of the fully densified Al_2O_3 ceramic.

Acknowledgments

This study was supported by the Basic Science Research Program through a grant from the National Research Foundation of Korea (NRF) funded by the Ministry of Education, Science and Technology (2011-0003144).

References

1. L.L. Hench, J. Am. Ceram. Soc. 81 (1998) 1705-1728.
2. A.N. Rascon, A.A. Elguezabal, E. Orrantia, and M.H. Bocanegra-Bernal, Int. J. Refract. Met. Hard Mater. 27 (2009) 962-970.
3. R.B. Heimann, in “Classic and advanced ceramics: from fundamentals to applications”, WILEY-VCH, 2010, p.25.
4. G. Willmann. Clin. Orthop. Relat. R 379 (2000) 173-177.
5. G. Willmann, and W.Von Chamier, in “Bioceramics in orthopedics: New applications”, Ferdinand Enke Verlag, 1998, p.19.
6. A.N. Rascon, A A. Elguezabal, E. Orrantia, and M.H. Bocanegra-Bernal, Int. J. Refract. Met. H 29 (2011) 333-340.
7. J. Wang, and R. Stevens, J. Mater. Sci. 24 (1989) 3421-3440.
8. F. Cesari, L. Esposito, F. M. Furgiuele, C. Maletta, and A. Tucci, Ceram. Int. 32 (2006) 249-255.
9. C. Santos, L. Teixeira, J. Daguano, S. Rogero, K. Strecker, and C. Elias, Ceram. Int. 35 (2009) 709-718.
10. S. Choi, and N. Bansal, Ceram. Int. 31 (2005) 39-46.
11. R.G. Luthardt, M.S. Holzhüter, H. Rudolph, V. Herold, and M.H. Walter, Dent. Mater. 20 (2004) 655-662.
12. H. Huang, Mater. Sci. Eng. A 345 (2003) 155-163.
13. DIN:51109, Prufung von keramischen Hochleistungs-werkstoffen, Ermittlung der Risszahigkeit K_{Ic}, Berlin: Beuth-Verlag (1991).
14. ISO: 6872, Biaxial flexure test (piston-on-three-ball test) and single edge V-notched beam method. 8 (2008) (E).
15. M. Asmani, C. Kermel, A. Leriche, and M. Ourak, J. Eur. Ceram. Soc. 21 (2001) 1081-1086.
16. J.W. Adams, R. Ruh, and K. Mazdiyasni, J. Am. Ceram. Soc. 80 (1997) 903-908.
17. W.D. Callister, in “Materials Science and Engineering: An Introduction, seventh ed”, John Wiley & Sons, 2007, p.257.
18. A.H. De Aza, J.Chevalier, and R. Torrecillas, Biomaterials. 23 (2002) 937-945.
19. A.G. Evans, J. Am. Ceram. Soc. 73 (1990) 187-206.
20. D. Tang, K.J. Lee, J. Xu, H.B. Lim, C.H. Lee, and W.S. Cho, Met. Mater. Int. 18 [3] (2012) 545-551.
21. K.K. Chawla, in “Ceramic Matrix Composites, first ed.”, Chapman&Hall, 1993. p.274.
22. Y. Cao and Eng. Fail. Anal. 8 (2001) 325-338.
23. J.P. Davim, and A.M. Baptista, J. Mater. Process. Technol. 103 (2000) 417-423.